A&A 553, A26 (2013)
DOI: 10.1051/0004-6361/201321084

Astronomy & Astrophysics

Refined physical properties and *g′*, *r′*, *i′*, *z′*, *J*, *H*, *K* transmission spectrum of WASP-23b from the ground⋆

N. Nikolov[1,2], G. Chen[1,3], J. J. Fortney[4], L. Mancini[1], J. Southworth[5], R. van Boekel[1], and Th. Henning[1]

[1] Max Planck Institute for Astronomy, Königstuhl 17, 69117 Heidelberg, Germany
e-mail: nikolay@astro.ex.ac.uk
[2] Astrophysics Group, School of Physics, University of Exeter, Stocker Road, EX4 4QL, Exeter, UK
[3] Purple Mountain Observatory & Key Laboratory for Radio Astronomy, 2 West Beijing Road, 210008 Nanjing, PR China
[4] Department of Astronomy & Astrophysics, University of California, Santa Cruz, CA 95064, USA
[5] Astrophysics Group, Keele University, Newcastle-under-Lyme, ST5 5BG, UK

Received 11 January 2013 / Accepted 14 March 2013

ABSTRACT

Context. Multi-band observations of planetary transits using the telescope defocus technique may yield high-quality light curves suitable for refining the physical properties of exoplanets even with small or medium size telescopes. Such observations can be used to construct a broad-band transmission spectrum of transiting planets and search for the presence of strong absorbers.
Aims. We have thoroughly characterised the orbital ephemeris and physical properties of the transiting planet and host star in the WASP-23b system, constructed a broad-band transmission spectrum of WASP-23 b and performed a comparative analysis with theoretical models of hot Jupiters.
Methods. We observed a complete transit of WASP-23 b in seven passbands simultaneously, using the GROND instrument on the MPG/ESO 2.2 m telescope at La Silla Observatory and telescope defocussing. The optical data were taken in the *Sloan g′*, *r′*, *i′* and *z′* passbands. The resulting light curves are of high quality, with a root-mean-square scatter of the residual as low as 330 parts per million (ppm) in the z'-band, with a cadence of 90 s. Near-infrared data were obtained in the *JHK* passbands. We performed a MCMC analysis of our photometry plus existing radial velocity data to refine measurements of the ephemeris and physical properties of the WASP-23 system. We constructed a broad-band transmission spectrum of WASP-23 b and compared it with a theoretical transmission spectrum of a hot Jupiter.
Results. We measured the central transit time with a precision ∼8 s. From this and earlier observations we obtain an orbital period of $P = 2.9444300 \pm 0.0000011$ d. Our analysis also yielded a larger radius and mass for the planet ($R_p = 1.067^{+0.045}_{-0.038}\ R_{Jup}$ and $M_p = 0.917^{+0.040}_{-0.039}\ M_{Jup}$) compared to previous estimates ($R_p = 0.962^{+0.047}_{-0.056}\ R_{Jup}$ and $M_p = 0.884^{+0.088}_{-0.094}\ M_{Jup}$). The derived transmission spectrum is marginally flat, which is not surprising given the limited precision of the measurements for the planetary radius and the poor spectral resolution of the data.

Key words. planetary systems – planets and satellites: atmospheres – planets and satellites: fundamental parameters – planets and satellites: general – stars: general

1. Introduction

The discovery and the detailed analysis of planets orbiting other stars can yield much information about their physical properties and evolutionary pathways. Since the first detection of a Jupiter-like planet hosted by a main sequence star (Mayor & Queloz 1995), several hundred exoplanets have been discovered via different methods. These comprise radial velocity (RV), astrometry, transits, microlensing, direct imaging and timing (see Schneider et al. 2011). Among the currently known exoplanets, those that transit their host stars command great interest because so many of their physical properties can be determined (Seager & Mallén-Ornelas 2003; Torres et al. 2010; Sozzetti et al. 2007). The properties of particular value include their radii and masses, and hence their surface gravities and mean densities. Observations of planetary transits currently provide the best route to constructing the mass−radius diagram of exoplanets, which brings critical information on the structure, formation and evolution of these worlds (Baraffe et al. 2010; Fortney et al. 2007; Burrows et al. 2007). Moreover, accurate measurements of the times of transit midpoints can allow the detection of additional bodies in known exoplanetary systems (Holman & Murray 2005) or alternatively may serve as a tool to verify the planetary nature and study the dynamical effect in multi-planet systems (Lissauer et al. 2011).

Notably, exoplanetary transits provide an opportunity to study the atmospheres of these objects. During transits part of the star light filters through the planetary atmosphere, and is imprinted with characteristic signatures of atomic (such as Na and K) and molecular (e.g. H_2O, CO and CH_4) absorption (Seager & Sasselov 2000; Hubbard et al. 2001).

The amount of irradiation incident upon giant extrasolar planets is an important factor in determining the properties of their atmospheres. One theory of giant exoplanets at high incident stellar fluxes predicts the existence of the pM and pL classes of hot Jupiters, depending on the presence of strong absorbers, such as gaseous TiO and VO in their atmospheres (Fortney et al. 2008, 2010). In particular, the increased opacity due to TiO and VO in the pM class should result in about a 3% variation of the

⋆ Based on observations collected with the Gamma Ray Burst Optical and Near-Infrared Detector (GROND) at the MPG/ESO-2.2 m telescope at La Silla Observatory, Chile. Programme 088.A-9006.

observed radius of a planet with a surface gravity of 15 m s^{-2}, over the wavelength interval 350–700 nm. For the purposes of transmission spectroscopy it is practical to convert these planet variations to the change of a directly observed quantity such as the transit depth $\delta = (R_p/R_*)^2$. Assuming a radius variation with an amplitude $n = 0.03$ (3%), the transit depth variation is defined as

$$\Delta\delta = \frac{\pi(R_p + nR_p)^2}{\pi R_*^2} - \frac{\pi R_p^2}{\pi R_*^2} \approx 2n\delta. \quad (1)$$

A transiting Jupiter orbiting a Sun-like star causes $\delta = 0.01$ which would translate into a variation of $\Delta\delta = 6 \times 10^{-4}$ (or $\Delta(R_p/R_*) = \sqrt{2n\delta} \approx 0.024$). Such precisions may be achieved by modelling light curves obtained using ground-based 2–4 m telescopes. The best results can be obtained by defocusing the telescope, which averages out sensitivity variations between the pixels on the detector and improves the observing efficiency by enabling a larger fraction of open-shutter time. However, the bandwidths of the filters used (which give the spectral resolution) is the other critical factor affecting the chances of detecting the signal in Eq. (1), similar to the detection of spectral features in spectrophotometry.

Several successful searches for the theoretically predicted strong absorbers in the optical and near-infrared (NIR) have been conducted first from space using the *Hubble* and *Spitzer* space telescopes, resulting in the detection of Na, CO, H_2O, CH_4 and Rayleigh scattering in the blue (Charbonneau et al. 2002; Pont et al. 2008; Sing et al. 2011b). Hampered by the atmosphere of the Earth (e.g. telluric contamination) and instrumental systematics, the ground-based detection of spectral features in exoplanet atmospheres took longer to yield results (Redfield et al. 2008; Snellen et al. 2008; Sing et al. 2011a, 2012).

Although transit photometry or spectrophotometry is often of high quality, the method pushes the limits of current instrumentation and has yielded controversial results (Swain et al. 2008; Beaulieu et al. 2011). The success of the method may also be hampered by the activity of the host star, in particular spot crossing events which can significantly increase the complexity of light curve analysis and lower the precision of the planetary radius measurement (Knutson et al. 2011).

The transiting hot Jupiter WASP-23 b orbits a moderately bright ($V = 12.68$) K1 V ($T_{\rm eff} = 5150 \pm 100$ K) star and was found by the SuperWASP survey (Triaud et al. 2011; Pollacco et al. 2006). The planet (radius $0.96 \pm 0.05\ R_J$, mass $0.88 \pm 0.10\ M_J$) has a 2.94 d circular orbit ($e < 0.062$ at the 3σ level).

In this paper we present ground-based simultaneous optical and NIR photometry of a transit of WASP-23 b. We refine its measured properties and orbital ephemeris. We then construct the first transmission spectrum of WASP-23 b and investigate the variation in radius of the planet with wavelength. The layout of the paper is as follows. In Sect. 2 we present the observations. Sect. 3 discusses our data reduction methods. In Sect. 4 we report the analysis of the data, measure the physical properties of the system, construct the planet's transmission spectrum, and compare this theoretical predictions. We conclude in Sect. 5.

2. Observations

We monitored the flux of WASP-23 (also known as GSC 07635-01376, $\alpha = 06^h44^m30.65^s$, $\delta = -42°45'41.0''$; J2000.0; $V = 12.68$ mag) during one transit on February 25, 2012 (Figs. 1 and 2). The data were collected using the GROND instrument,

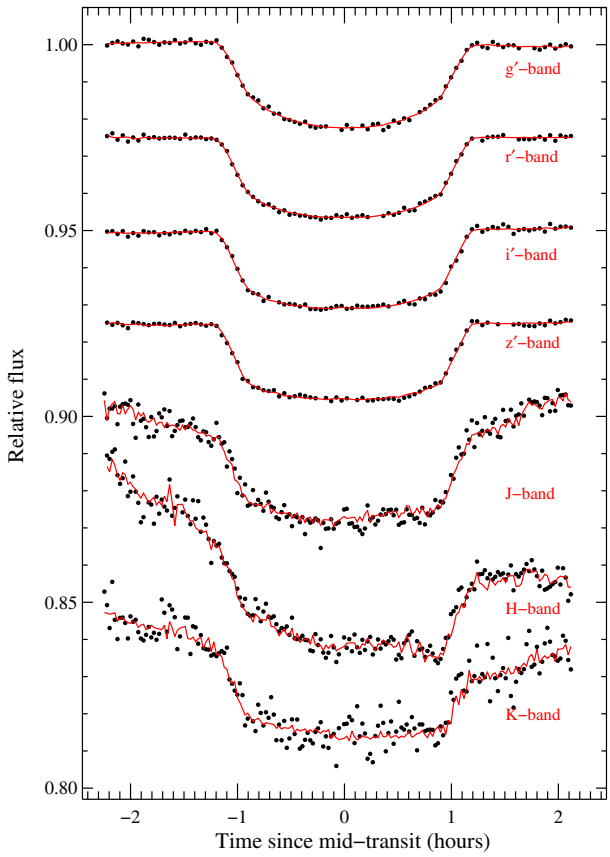

Fig. 1. Simultaneous optical to near-infrared (*Sloan* g', r', i', $'z$ and *Johnson* J, H, K) raw transit light curves of WASP-23 (dots), obtained with GROND on UT February 25, 2012 an the corresponding correction functions (red lines).

attached to the MPG/ESO 2.2 m telescope at ESO La Silla Observatory (Chile)[1]. GROND (Gamma Ray Burst Optical and Near-Infrared Detector) is a simultaneous multi-channel imager that has been specifically designed for gamma-ray burst (GRB) afterglow observations (Greiner et al. 2008). Its capability to simultaneously monitor sources in seven optical to NIR passbands make it an excellent instrument for obtaining high quality, multi-band transit light curves. It is capable of yielding light curves with a root-mean-square (rms) scatter better than 1 mmag, depending on the atmospheric conditions (Lendl et al. 2010; Nikolov et al. 2012; Mancini et al. 2013a).

To reach GROND's detectors the light from the telescope is split using dichroics into seven beams, resulting in response curves close to the Sloan g' ($\lambda = 459$ nm), r' ($\lambda = 622$ nm), i' ($\lambda = 764$ nm), z' ($\lambda = 899$ nm) in the optical and J ($\lambda = 1256$ nm), H ($\lambda = 1647$ nm) and K ($\lambda = 2151$ nm) bands in the NIR, respectively. The optical beams are incident onto four 2048×2048 back-illuminated E2V CCDs with $5.4' \times 5.4'$ fields of view (FOVs) at a plate scale of $0.''158$ pixel^{-1}. The NIR channels are imaged onto three 1024×1024 Rockwell HAWAII-1 arrays with 10×10 arcmin FOVs and plate scales $0.''6$ pixel^{-1}. The off-axis guide camera was used to autoguide the telescope.

Light curves were acquired in GROND's non-dither mode to decrease systematics associated with inter-pixel sensitivity variations. We obtained data for WASP-23 and eleven and seven

[1] Detailed information on the 2.2 m telescope, the GROND instrument and the relevant technical settings can be found at http://www.eso.org/sci/facilities/lasilla/telescopes/2p2/

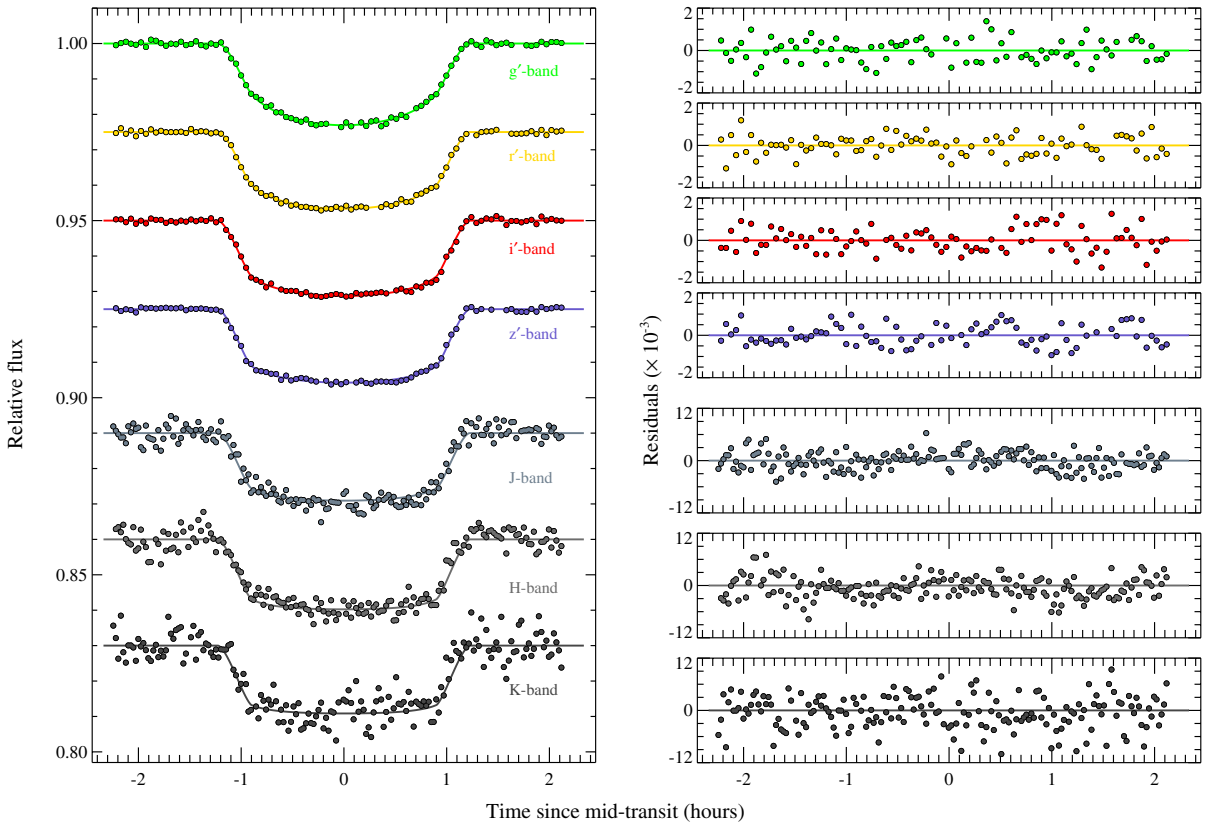

Fig. 2. *Left panel*: detrended transit light curves (dots) of and the best-fit models (lines) for the WASP-23 GROND data. The optical photometry clearly exhibits a change in the shape of the transit due to the different limb-darkening in each band. *Right panel*: residuals of the light curve compared to the fitted models.

Table 1. Instrumental and observational settings used to obtain data for WASP-23 (median values), during the observation on UT February 25, 2012.

GROND band	Gain (ADU)	$d_{\rm ring}{}^a$ (pixel)	Max count (ADU) $\times 10^3$	Background^b (ADU) $\times 10^3$
g'	1.45	57	18.6	0.3
r'	1.33	67	43.8	0.3
i'	1.62	51	27.2	0.3
z'	1.74	48	22.3	0.4
J	2.39	9	26.7	5.0
H	2.65	6	18.2	17.0
K	2.55	24	13.1	11.0

Notes. $^{(a)}$ Diameter of the defocussed PSF ring in pixels. $^{(b)}$ Measured using an annulus, centered on the stellar PSF, encompassing an area four times larger than the area used to produce a photometric measurement of the stellar PSF.

reference stars in the optical and NIR images, respectively. We applied a moderate defocus to the 2.2 m telescope, such that the point spread functions (PSFs) had diameters ~76 pixels (12″) in the optical and ~13 pixels (7.″6) in NIR. Table 1 gives details of the instrumental setup and illumination levels of the seven beams. As the guide camera was also defocussed, we made sure in advance that at least one bright star was within its FOV.

The main advantages of the telescope defocus technique have been discussed by several researchers, e.g. Winn et al. (2007), Gillon et al. (2007), Southworth et al. (2010, and references therein), Croll et al. (2010). Although the method results in non-uniformly defocused PSFs of the stars across large FOVs (≥1° × 1°), the technique performs well on small FOVs (such as GROND). It allows superb PSF sampling, significantly reducing the random and systematic errors resulting from detector imperfections and response variations. The technique also avoids detector saturation due to fluctuations in seeing, because such fluctuations are small compared to the level of defocusing. We note that telescope defocusing is not well suited to photometry in crowded fields or when the target star has nearby companions. We used the 2MASS catalogue to rule out these possibilities for our observations of WASP-23.

We observed WASP-23 on February 25, 2012 for 4.4 h from UT $00^{\rm h}32^{\rm m}$ to $04^{\rm h}56^{\rm m}$. An exposure time of 90 s was used in the optical and resulted in 91 integrations. The slow read-out mode was selected (~48 s read-out-time) as it delivers high-quality images[2]. In the NIR averaged stacks of seven 10 s integrations were obtained to improve the signal-to-noise ratio (S/N), resulting in a total of 181 images. At the beginning of the observation the airmass of the target began at 1.04, peaked at 1.03, and increased to 1.47 by the end of the observing sequence. The observing conditions were nearly photometric, with seeing variation from ~16 to ~18 pixels as measured from a fit to the wings of the defocused PSFs.

Theoretical models of exoplanet transmission spectra imply that the NIR region is richer than the optical in terms of potential spectroscopic signatures. We therefore aimed to obtain high-precision light curves for that region as well. The control

[2] The GROND detector can also be read-out in "fast" mode (~11 s read-out-time), but it has been found during previous transit observations that images obtained in that mode suffer from systematic effects that lower the quality of the resulting light curves.

of GROND allows only a single integration time (limited from 0 to 10 s) for the three JHK bands simultaneously, so we optimised the exposure time such that the highest S/N was obtained for the band when the star had the most flux (J). For the degree of telescope defocus, we aimed to optimise the S/N in the optical, as we expected better performance in that region based on previous experience (Nikolov et al. 2012; Mancini et al. 2013a).

3. Data reduction and analysis

The data were reduced and analysed on a channel-by-channel basis, using a customised pipeline. GROND's optical and NIR data are provided in separate fits files. The images from the optical channels are packed into four-extension data cubes and the JHK read-outs are delivered as a single 3072×1024 image. After processing to collapse the optical data cubes and to split each NIR image, the data were sorted into science and calibration images.

For the optical data a median-combined master bias frame was computed using 20 zero-second images. We estimated the average dark current of GROND's optical detectors to be ~0.01 $e^- s^{-1}$ pixel^{-1}, which is negligible for our data. We therefore neglected the dark current correction. A median-combined master flat-field was calculated using six bias-corrected and dithered twilight sky flat-fields that survived a selection criterion for linearity in each of the passbands. Finally, each optical science frame was de-biased and flat-field corrected to produce calibrated time series of images.

In the NIR, a series of ten dark frames with integration time of 10 s were employed to compute a median-combined master dark frame. A series of 24 dithered twilight sky flat frames were used to obtain a median-combined master sky flat. The master dark frame was subtracted from all the science and sky flat frames. Each dark-subtracted science image was then corrected with the master sky flat frame. An electronic odd-even readout pattern along the y-axis was removed before flat-fielding. This was done by smoothing each image and comparing it with the unsmoothed one after the master dark had been subtracted. The amplitudes of the read-out pattern were then determined by comparing the median level of each column to the overall median level. Each column was then shifted to the overall median level. The master sky flats were divided out from the science images after removal of the read-out pattern.

Previous investigators have commonly obtained dithered images prior to the main observing sequence to further correct the science images against sky background variations. However, similar corrections are inadequate for sky gradients that vary on timescales less than the duration of the observations. In addition, relative photometry, if performed at gradient-stable sky backgrounds is in practice insensitive to sky variations that concern simply the sky level. Finally, previous analyses of WASP-44 b (Mancini et al. 2013a) with and without sky corrections resulted in indistinguishable light curves with similar scatter. We therefore did not obtain dithered sky images.

We performed circular aperture photometry on each of the calibrated images. To accurately determine the central positions of the heavily defocused PSFs, we proceeded as follows. First, we extracted sub-images, roughly centred on each star. The brightest stars were rings with typical diameters ~50 and ~15 pixels in the optical and NIR, respectively. We then convolved each image with a Gaussian kernel to produce a smoothed PSF with a well-defined peak, located at the centre of the original PSF. Finally, we fitted a two-dimensional Gaussian to measure the PSF centre and full width at half maximum, which was latter used to monitor the seeing variations during the observation. Instrumental fluxes and uncertainties (computed taking into account a random photon noise) were acquired using a DAOPHOT-type photometry algorithm as implemented in the IDL[3] APER[4] routine.

Table 2. r'-band light curve extract.

BJD[a]	Flux	$\sigma_{\rm Flux}$[b]	z[c]	x[d]	y[e]
2.52787	1.000410	0.000256	1.03539	7.73	71.17
2.52990	1.001160	0.000269	1.03370	7.61	70.30
2.53193	0.999446	0.000253	1.03274	7.54	70.06
2.53396	1.000615	0.000255	1.03170	6.95	70.66
2.53599	0.998938	0.000253	1.03100	6.72	70.67
2.53802	1.000043	0.000252	1.03079	6.18	69.93

Notes. [(a)] BJD – 2 455 980; [(b)] 1-σ error-bar of the flux, as measured by APER; [(c)] airmass; [(d)] x – 630 horizontal pixel position of the defocussed PSF; [(d)] y – 1300 vertical pixel position of the defocussed PSF.

Table 3. Theoretical limb-darkening coefficients, light curve residual scatter (in parts per million, ppm) and the β-factor used to estimate the photometric uncertainties of the GROND data.

GROND band	u_1	u_2	rms (ppm)	β
g'	0.7413	0.0719	419	1.00
r'	0.5323	0.1804	371	1.00
i'	0.4224	0.1983	430	1.27
z'	0.3491	0.2062	330	1.28
J	0.1063	0.2589	1480	1.50
H	0.1126	0.3130	1760	1.52
K	0.2389	0.2467	2980	1.16

To compute the relative flux light curve of WASP-23 in the four optical channels we used 2MASS J06444546-4242083 as a comparison star. Because of the relatively small FOV of GROND we performed an exhaustive investigation of the possible reference stars prior to the observations. This object satisfied the requirements, being isolated enough to avoid contamination with bright neighbours when defocused, and being the only stellar source in the optical FOV of a similar brightness and colour to WASP-23, thus reducing systematic effects due to differential colour extinction. For instance, the instrumental magnitude differences (WASP-23 minus comparison star), measured on UT Februray 25 2012 were $\Delta g' = 0.510$ mag, $\Delta r' = 0.082$ mag, $\Delta i' = 0.319$ mag, $\Delta z' = 0.785$ mag. For the same reasons, in the NIR channels we used 2MASS J06445925-4245061 as the comparison star. The instrumental magnitude differences were $\Delta J = -0.784$ mag, $\Delta H = -0.696$ mag and $\Delta K = -0.396$ mag.

To select optimum sizes for the inner aperture and sky annulus we investigated the root-mean-square (rms) of the out-of transit baseline flux as a function of various combinations of aperture and annulus sizes. Table 2 exhibits an r'-band light curve extract along with the airmass and measurements of the (x, y) drift of the PSF on the detector employed to correct the light curve during the analysis.

We used the UT time stamps available in the fits headers of the data and computed the central times of each integration using

[3] The acronym IDL stands for Interactive Data Language. For further details see http://www.exelisvis.com/ProductsServices/IDL.aspx

[4] Part of APER Astronomy User's Library. For detailed information see http://idlastro.gsfc.nasa.gov/

the exposure times. All times were then converted to Barycentric Julian Date (BJD), using the converter of Eastman et al. (2010).

4. Light curve analysis

We performed the light curve analysis in two steps. First, we simultaneously fitted the seven optical to NIR GROND light curves to derive accurate estimates of the transit central time T_c and orbital period P, and evaluated the orbital parameters and planetary radius (i, a/R_*, R_p/R_*).

In the second step we complemented the GROND photometry with the radial velocity (RV) measurements of WASP-23, reported by Triaud et al. (2011) and performed a joint photometry plus RV MCMC analysis using EXOFAST (Eastman et al. 2013). As our ultimate goal is to construct a ground-based transmission spectrum of WASP-23, based on uniform transit parameters from all bands we excluded the RVs obtained during transit, which are affected by the Rossiter-McLaughlin effect.

As EXOFAST allows an analysis of one light curve at a time we use the results from the first step (the simultaneous fit to the photometry) as priors for EXOFAST. The latter was used to derive reliable estimates of the physical properties and their uncertainties for WASP-23 b and its parent star. EXOFAST utilizes empirical polynomial relations (Torres et al. 2010) between the masses and radii of stars, and their surface gravities ($\log g$), effective temperatures ($T_{\rm eff}$) and metallicities [Fe/H], based on a large sample of well-studied non-interacting binaries. Including this empirical relation as a constraint allows a derivation of the full orbital and physical properties from transit light curves and RV data (Eastman et al. 2013).

In the first step, we modelled the transit light curves simultaneously in flux units). A two-component correction function was constructed, containing a transit model multiplied by a baseline function that accounts for the most significant known systematic effects affecting ground-based transit observations: airmass and detector intra-pixel sensitivity variations (Fig. 1).

The first component is based on the analytical transit models of Mandel & Agol (2002), which in addition to the transit central time (T_c) and orbital period (P) is a function of the orbital inclination (i), planet semi-major axis and radius normalized to the stellar radius (a/R_*) and (R_p/R_*), respectively. To account for the limb darkening of the star we adopted the quadratic limb darkening law:

$$\frac{I_\mu}{I_1} = 1 - u_1(1-\mu) - u_2(1-\mu)^2, \quad (2)$$

where I is the intensity and μ is the cosine of the angle between the line of sight and the normal to the stellar surface. We fixed the two limb darkening coefficients (u_1 and u_2) to their theoretical values (see Table 3 for details), which we obtained by interpolating within the calculated and tabulated ATLAS models (Claret & Bloemen 2011; Eastman et al. 2013) to the stellar parameters $T_{\rm eff} = 5150 \pm 100$ K, $\log g = 4.4 \pm 0.2$ (cgs), [Fe/H] $= -0.05 \pm 0.13$ and $v_t = 0.8 \pm 0.3$ km s^{-1}, which we adopted from Triaud et al. (2011).

We constructed a baseline function to account for systematic effects that concern the (in- and out-of-transit) photometry. It contains a linear airmass (z) term as well as a quadratic polynomial of the PSF location (x, y) on the detector to take into account for any inter-pixel sensitivity variations:

$$F(z,x,y) = 1 + a_0 + a_1 z + a_2 x + a_3 x^2 + a_4 y + a_5 y^2 + a_6 xy. \quad (3)$$

To derive the best-fit parameters we employed the Levenberg-Marquardt least-squares algorithm, minimising the χ^2 function over the data (Fig. 2) (Markwardt 2009). Conveniently, EXOFAST also takes into account the systematics, incorporating a baseline function and trends, as described in Eastman et al. (2013). We therefore included function (3) in EXOFAST to take into account the systematics and to enable a uniform analysis of the in- and out- of-transit photometry[5].

An accurate derivation of system parameters from transit light curve fits requires a realistic estimation of the related photometric errors. The photometric uncertainties produced by IDL/APER are usually underestimates, so we ignored them in our analysis. These are formal statistical uncertainties and do not take into account time-correlated noise. We used the out-of-transit data of each light curve before detrending and applied the "time-averaging" procedure proposed by Pont et al. (2006) and used by various authors including Gillon et al. (2006), Winn et al. (2007, 2008), Gibson et al. (2008), Nikolov et al. (2012), Southworth et al. (2012a,b) and Mancini et al. (2013b) to inflate the photometric errors to more realistic values. In summary, for each band we computed the β-ratio between the standard deviation of the out-of-transit unbinned and binned data with bin sizes similar to the transit ingress/egress duration. The photometric uncertainties were therefore set to the out-of-transit unbinned standard deviation multiplied by the corresponding β-factor (see Table 3).

4.1. System parameters

To derive system parameters for WASP-23, including the priors for EXOFAST, we relied on the light curves from the seven GROND passbands. We assumed that i and a should not depend on the observed band and constrained them to a single universal value. In contrast, we treated the planetary radius as a free parameter for each passband. We also set the linear and the quadratic limb darkening coefficients to their theoretical values as well as the initial guess for the orbital period to the value reported in Triaud et al. (2011). We found $i = 88.02° \pm 0.19°$, $a/R_* = 9.94 \pm 0.11$ and ratios of the radii for each passband: $R_p/R_*(g') = 0.13410 \pm 0.00066$, $R_p/R_*(r') = 0.13348 \pm 0.00049$, $R_p/R_*(i') = 0.13455 \pm 0.00047$, $R_p/R_*(z') = 0.13439 \pm 0.00048$, $R_p/R_*(J) = 0.1340 \pm 0.0016$, $R_p/R_*(H) = 0.1352 \pm 0.0016$, $R_p/R_*(K) = 0.1325 \pm 0.0020$. These values were input in EXOFAST as priors along with the star's $T_{\rm eff}$, $\log g$ and [Fe/H], fitting the transit photometry and RVs simultaneously in each band. The results for the main physical properties are summarised in Tables 4 and 5. Our results are slightly different from these reported in Triaud et al. (2011), though with higher precision, favouring a more inflated planet. In particular we improved the precision of i by factors of ~4 and ~6.5 for the lower and upper limits, respectively. We find the radius of WASP-23b to be $R_p = 1.067^{+0.045}_{-0.038}\ R_{\rm Jup}$, which is larger than the radius presented in the discovery paper.

4.2. Ephemeris

One of our main goals was to secure the transit ephemeris (T_c and P) of WASP-23 b. We fixed all physical parameters to their values derived in the previous section and fitted GROND's light

[5] We choose to employ MPFIT in the first step as it allows one to construct a joint model incorporating the entire dataset. In contrast EXOFAST permits an analysis on a per-channel basis, i.e. one band at a time. We therefore, determined universal values for a/R_*, i, T_c, P and R_p/R_* using the complete dataset and used these results as priors in EXOFAST, where the fitting is done for each band.

Table 4. Derived system parameters for WASP-23 b from light curve fits, compared to the corresponding results reported in the discovery paper.

Band	R_p/R_*	i°	a/R_*
GROND g'	$0.13402^{+0.00062}_{-0.00061}$	$87.93^{+0.24}_{-0.22}$	$9.900^{+0.14}_{-0.14}$
GROND r'	$0.13336^{+0.00045}_{-0.00044}$	$87.85^{+0.22}_{-0.21}$	$9.850^{+0.14}_{-0.13}$
GROND i'	$0.13433^{+0.00044}_{-0.00043}$	$88.02^{+0.30}_{-0.26}$	$9.910^{+0.17}_{-0.16}$
GROND z'	$0.13400^{+0.00042}_{-0.00041}$	$87.83^{+0.25}_{-0.24}$	$9.850^{+0.15}_{-0.15}$
GROND J	$0.1340^{+0.0012}_{-0.0011}$	$88.12^{+0.93}_{-0.74}$	$10.24^{+0.44}_{-0.49}$
GROND H	$0.13520^{+0.0012}_{-0.0012}$	$87.75^{+0.91}_{-0.70}$	$9.970^{+0.56}_{-0.52}$
GROND K	$0.1326^{+0.0014}_{-0.0014}$	$88.74^{+0.85}_{-1.0}$	$10.59^{+0.32}_{-0.63}$
Weighted mean	$0.13394^{+0.00022}_{-0.00022}$	$87.91^{+0.12}_{-0.11}$	$9.893^{+0.071}_{-0.070}$
Triaud et al. (2011)	$0.13004^{+0.00040}_{-0.00045}$	$88.39^{+0.79}_{-0.45}$	10.61

Notes. The final estimates of our analysis are the weighted mean values from all bands.

curves simultaneously to derive a transit time. We added this to all reported central transit times in the literature (Table 6), then performed a linear fit as a function of the observed epoch (E):

$$T_C(E) = T_o + E \times P. \quad (4)$$

We derived $P = 2.9444300 \pm 0.0000011$ d and $T_c = 2\,454\,813.68159 \pm 0.00042$ BJD. This period is in poor agreement ($\sim 3\sigma$ level) with the value reported in Triaud et al. (2011) ($P = 2.9444256^{+0.0000011}_{-0.0000013}$ d), but is more reliable due to the larger time span of transit times we used. We investigated the observed minus calculated (O–C) residuals of the timings versus our ephemeris. We found no systematic deviation and conclude that there is no compelling evidence for transit timing variations (Fig. 3).

4.3. Radius variation

A set of simultaneous multi-band transit light curves provides an opportunity to investigate the behaviour of the measured planetary radius with wavelength. Atmospheric absorption features in the optical regime due to sodium (Na) and potassium (K) have been theoretically predicted (Seager & Sasselov 2000) and observed in the transmission spectra of hot Jupiters, e.g. XO-2b (Sing et al. 2011b, 2012) from the ground. Contrary to this example of an agreement between theory and observation, an analysis of HST ultraviolet-optical spectrophotometric data of HD 189733 b by Sing et al. (2011a) revealed a featureless spectrum, which might be an indication for the presence of high altitude clouds. These observational results indicate the diversity of exoplanet atmospheres, the understanding of which requires more observational results.

To investigate the radius variation of WASP-23 b in GROND's passbands we fixed P, i and a/R_* to their final results from the analysis in Sect. 4.1, and the linear and quadratic limb darkening coefficients to their predicted values. We fitted for the planetary radius (specifically the ratio of the radii R_p/R_*) and the instrumental systematics. This approach improves the precision of the measured planetary radius, by avoiding sources of uncertainty common to all measurements of R_p/R_*. In addition, the fit takes into account the information for the system parameters and reflects differences in the transit depth that are determined only by the size of the planet in each passband. To estimate realistic values for the normalised planet radii and their error bars we carried out the fitting using an MCMC approach. The results for the planet radii, obtained at this step are displayed in Figs. 4 and 5. The vertical error bars comprise the 68.3% confidence levels from the MCMC distributions of R_p/R_*. As expected, the radius measurements in the optical regime show much smaller error bars compared to the NIR passbands. This is due to the lower scatter of the data in the optical. We also show horizontal bandwidths (plotted with error-like bars) that have been computed as the full widths at half maximum, using GROND's filter curves, which are indicated at the lower part of the plot.

To compare our observational results with theorical predictions we employed the system parameters from Table 5 and computed a 1D model atmosphere of WASP-23 b, using the code described in Fortney et al. (2005, 2008). The fully non-gray model uses the chemical equilibrium abundances of Lodders & Fegley (2002) and the opacity database described in Freedman et al. (2008). The atmospheric pressure-temperature profile simulates planet-wide average conditions. We computed the transmission spectrum of the model using the methods described in Fortney et al. (2010). For each of the GROND passbands we computed the expected theoretical value given the synthetic transmission spectrum, integrating over the corresponding filter curve. Finally, we used the derived theoretical values for the planet radius and fitted them as a model to the measured values of R_p/R_* from the seven GROND light curves (Figs. 4 and 5). We find a good agreement between the observationally derived measurements and synthetic values of the planetary radii, consistent with a featureless transmission spectrum at the $\sim 1\sigma$ level. Two of our radius estimates (r'-band in the optical and H-band in the NIR) were found to be off by slightly more than 1σ from their corresponding theoretical values. This is most likely due to systematics of unknown origin.

5. Summary and discussion

We have presented observational results based on data collected with the GROND instrument on the MPG/ESO 2.2 m telescope at ESO La Silla, during one transit of the hot Jupiter WASP-23 b, the first photometric follow-up of this object after its discovery. We employed the telescope defocusing technique and autoguiding to optimise the quality of the light curve and minimise the instrumental systematics in the complete optical to NIR capability of the GROND instrument for the first time. Light curves constructed from this data set showed a scatter versus fitted models as low as 330 ppm (Table 3). For comparison, a recent observation performed by Tregloan-Reed & Southworth (2013) with the 3.58 m New Technology Telescope (NTT), in defocussed mode obtained light curve scatters of 258 and 211 ppm, during two transit events of WASP-50 b. Their lower scatter is expected due to the larger aperture of the telescope.

We used the full potential of GROND's optical to NIR dataset to refine the ephemeris and system parameters of the WASP-23b system and compared our results with these presented by Triaud et al. (2011). We complemented our photometric data with existing RV measurements of the parent star to derive the full physical properties of the system. We measured the central transit time with a precision ~ 8 s, complemented this measurement with published transit epochs, and refined the orbital period of WASP-23 b. We analysed the O–C diagram of the transit times and found no significant evidence for transit timing variations. Using all of the seven GROND bands we determined a larger and more precise value for the radius of WASP-23 b, which is in agreement at the $\sim 2\sigma$ level with that from Triaud et al. (2011). The latter however, was derived based on a joint fit

Table 5. Stellar and planetary parameters for WASP-23 derived from light curve and RV fits to the GROND photometry and RV measurements from Triaud et al. (2011).

Quantity	Symbol	This work	Triaud et al. (2011)
Stellar parameters			
Mass ($M_\odot$)	M_*	$0.842^{+0.051}_{-0.049}$	$0.78^{+0.13}_{-0.12}$
Radius ($R_\odot$)	R_*	$0.819^{+0.033}_{-0.028}$	$0.765^{+0.033}_{-0.049}$
Luminosity ($L_\odot$)	L_*	$0.421^{+0.053}_{-0.046}$	–
Density (cgs)	ρ_*	$2.112^{+0.046}_{-0.044}$	$1.843^{+0.025}_{-0.027}$
Surface gravity (cgs)	$\log(g_*)$	$4.531^{+0.025}_{-0.029}$	4.4 ± 0.2
Effective temperature (K)	$T_{\rm eff}$	5149^{+93}_{-93}	5150 ± 100
Metallicity	[Fe/H]	$-0.06^{+0.13}_{-0.13}$	-0.05 ± 0.13
Planetary parameters			
Semi-major axis (AU)	a	$0.03798^{+0.00075}_{-0.00075}$	$0.0376^{+0.0016}_{-0.0024}$
Mass ($M_{\rm J}$)	$M_{\rm P}$	$0.917^{+0.040}_{-0.039}$	$0.884^{+0.088}_{-0.099}$
Radius ($R_{\rm J}$)	$R_{\rm P}$	$1.067^{+0.045}_{-0.038}$	$0.962^{+0.047}_{-0.056}$
Density (cgs)	$\rho_{\rm P}$	$0.916^{+0.096}_{-0.102}$	–
Surface gravity	$\log(g_{\rm P})$	$3.294^{+0.027}_{-0.031}$	–
Equilibrium temperature[a] (K)	$T_{\rm eq}$	1152^{+28}_{-26}	–
Safronov Number	Θ	$0.0770^{+0.0033}_{-0.0035}$	–
Incident flux (10^9 erg s^{-1} cm^{-2})	$\langle F \rangle$	$0.400^{+0.040}_{-0.035}$	–
Orbital period (day)	P	2.9444300 ± 0.0000011	$2.9444256^{+0.0000011}_{-0.0000013}$
Reference transit time (BJD)	T_0	$2\,454\,813.68159 \pm 0.00042$	$2\,455\,320.12363^{+0.00012}_{-0.00013}$
RV parameters			
RV semi-amplitude (m/s)	K	$145.57^{+2.44}_{-2.49}$	–
Mass ratio	$M_{\rm P}/M_*$	$0.001039^{+0.000027}_{-0.000027}$	–

Notes. [(a)] Assuming a little redistribution over the surface of the planet, i.e., the area that is reemitting with average temperature $T_{\rm eq}$ is $2\pi R_{\rm p}^2$, as in Hansen & Barman (2007).

Table 6. Transit mid-times and O–C residuals computed using transit light curves from the literature and the observation reported in this work.

Epoch	Central time ($\rm BJD_{TDB}$)	O–C (days)	Reference
0	$2\,454813.68163^{0.00070}_{0.00073}$	0.000044	1
98	$2\,455\,102.23664^{0.00065}_{0.00068}$	0.000916	1
143	$2\,455\,234.73568^{0.00075}_{0.00079}$	0.000607	1
251	$2\,455\,552.73321^{0.00030}_{0.00030}$	–0.000300	1
254	$2\,455\,561.56610^{0.00052}_{0.00051}$	–0.000700	1
397	$2\,455\,982.620315^{0.000097}_{0.000097}$	0.000028	2

Notes. Note the high precision (~8 s) of the the transit time derived using GROND's light curves. 1– Triaud et al. (2011); 2– this work.

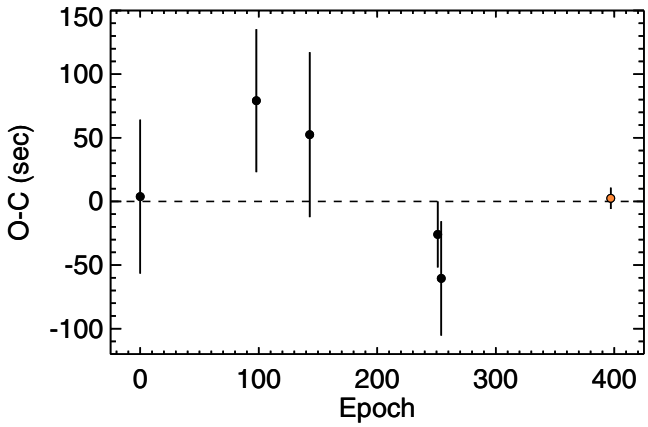

Fig. 3. Observed minus computed (O–C) transit times for WASP-23 b, using observations reported in the literature (black dots) and our measurement (orange dot), compared to a linear ephemeris (dashed line).

to five lower-quality light curves covering the z, R and $I+z$ passbands. Despite our larger value for the planetary radius, WASP-23 b still sits below the region of the so-called heavily "*bloated*" hot Jupiters, in accord to the theoretical models for irradiated giant planets of Baraffe et al. (2008). Moreover, Fortney et al. (2007) presented theoretical mass-radius relationships for irradiated giant exoplanets, parametrized by mass, age, and an effective orbital distance, defined as the distance from the Sun, where a hypothetical planet would receive the same flux as the actual planet. Given the luminosity of WASP-23 and the semi-major axis of its planet we evaluated that distance to be $a = 0.585$ AU. We then interpolated the models of Fortney et al. (2007) to match the distance and the mass of WASP-23b for a solar composition at 4.5 Gyr and evaluated $R_{\rm p} = 1.042\ R_{\rm Jup}$, which is within the error of our result.

Finally, we used the potential of the GROND light curves to investigate the (possible) variation of the planetary radius with wavelength and constructed a ground-based simultaneous optical to NIR broad-band transmission spectrum of WASP-23 b. According to our results for the system parameters (Table 5) the equilibrium temperature of WASP-23 b is $T_{\rm eq} = 1152^{+28}_{-26}$ K, which places the planet among the pL-class (cooler) of giant

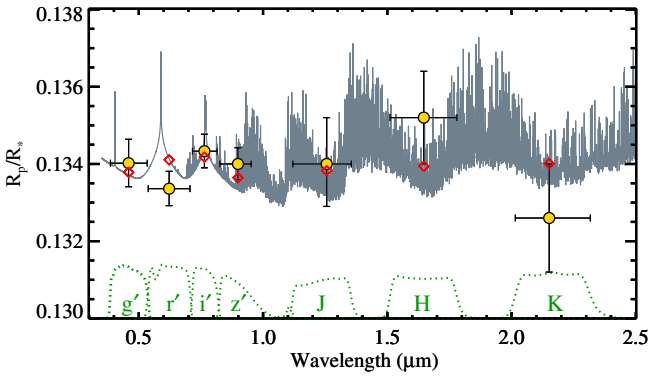

Fig. 4. Radius variation (measured with R_p/R_* and indicated with yellow disks with error bars) of WASP-23 b in the seven optical to NIR passbands, compared to a synthetic transmission spectrum based on a planet-wide pressure-temperature profile (grey continuous line). The open red diamonds indicate the expected theoretical values, integrated over GROND's filter curves. The latter are displayed as dotted lines at the origin of the graph.

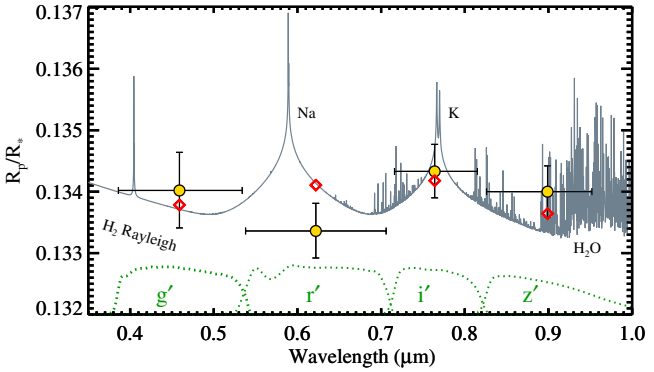

Fig. 5. Same as Fig. 4, but displaying a closer view of the radius variation in the optical bands.

close-in exoplanet atmospheres in the scheme proposed by Fortney et al. (2008). Taking into account these results, we generated a synthetic atmospheric transmission model of an irradiated hot Jupiter, assuming a planet-wide pressure-temperature profile and compared theory with observations. The optical part of the synthetic transmission spectrum at this equilibrium temperature and surface gravity (20.73 m s^{-2}) suggests a radius variation due to the presence of gaseous sodium and potassium in the atmosphere of WASP-23 b, while the NIR parts are dominated by water vapour features. The detection of such radius variation should be a realistic task, if observations could be taken at the precision levels attained in this work and with a higher spectral resolution. However, even the narrowest passband of GROND (i'-band) spans ∼120 nm, which effectively reduces the sensitivity of our measurements to radius variations. This effect is illustrated in Figs. 4 and 5, where using the filter curves of GROND we computed the theoretically expected values for the radius of WASP-23 b, given the synthetic spectrum. We fitted our observational result for the radius to the theoretical estimates. Although we found the r'-band, which covers the expected sodium absorption line, to deviate from the predicted theoretical value, overall the theoretical model is in very good agreement with observational transmission spectrum at the $\sim 1\sigma$ level.

Acknowledgements. The authors acknowledge Timo Anguita and Régis Lachaume for their technical support at the time of the observations, David Sing and Frédéric Pont for their constructive discussions as well as the anonymous referee for the detailed and constructive suggestions that improved the manuscript. N.N. acknowledges support from an STFC consolidated grant. J.S. acknowledges STFC for the award of an Advanced Fellowship.

References

Baraffe, I., Chabrier, G., & Barman, T. 2008, A&A, 482, 315
Baraffe, I., Chabrier, G., & Barman, T. 2010, Rep. Prog. Phys., 73, 016901
Beaulieu, J.-P., Tinetti, G., Kipping, D. M., et al. 2011, ApJ, 731, 16
Brogi, M., Snellen, I. A. G., de Kok, R. J., et al. 2012, Nature, 486, 502
Burrows, A., Hubeny, I., Budaj, J., & Hubbard, W. B. 2007, ApJ, 661, 502
Charbonneau, D., Brown, T. M., Noyes, R. W., & Gilliland, R. L. 2002, ApJ, 568, 377
Claret, A., & Bloemen, S. 2011, A&A, 529, A75
Croll, B., Albert, L., Lafreniere, D., et al. 2010, ApJ, 717, 1084
Eastman, J., Silverd, R., & Gaudi, B. S. 2010, PASP, 122, 935
Eastman, J., Gaudi, B. S., & Agol, E. 2013, PASP, 125, 83
Fortney, J. J., Marley, M. S., Lodders, K., Saumon, D., & Freedman, R. 2005, ApJ, 627, L69
Fortney, J. J., Marley, M. S., & Barnes, J. W. 2007, ApJ, 659, 1661
Fortney, J. J., Lodders, K., Marley, M. S., & Freedman, R. S. 2008, ApJ, 678, 1419
Fortney, J. J., Shabram, M., Showman, A. P., et al. 2010, ApJ, 709, 1396
Freedman, R. S., Marley, M. S., & Lodders, K. 2008, ApJS, 174, 504
Gibson, N. P., Pollacco, D., Simpson, E. K., et al. 2008, A&A, 492, 603
Gillon, M., Pont, F., Moutou, C., et al. 2006, A&A, 459, 249
Gillon, M., Pont, F., Demory, B.-O., et al. 2007, A&A, 472, L13
Greiner, J., Bornemann, W., Clemens, C., et al. 2008, PASP, 120, 405
Hansen, B. M. S., & Barman, T. 2007, ApJ, 671, 861
Holman, M. J., & Murray, N. W. 2005, Science, 307, 1288
Hubbard, W. B., Fortney, J. J., Lunine, J. I., et al. 2001, ApJ, 560, 413
Knutson, H. A., Madhusudhan, N., Cowan, N. B., et al. 2011, ApJ, 735, 27
Lendl, M., Afonso, C., Koppenhoefer, J., et al. 2010, A&A, 522, A29
Lissauer, J. J., Fabrycky, D. C., Ford, E. B., et al. 2011, Nature, 470, 53
Lodders, K., & Fegley, B. 2002, Icarus, 155, 393
Mancini, L., Nikolov, N., Southworth, J., et al. 2013a, MNRAS, in press [arXiv:1301.3005]
Mancini, L., Southworth, J., Ciceri, S., et al. 2013b, A&A, 551, A11
Mandel, K., & Agol, E. 2002, ApJ, 580, L171
Markwardt, C. B. 2009, Astronomical Data Analysis Software and Systems XVIII, Quebec, Canada, eds. D. Bohlender, P. Dowler, & D. Durand (San Francisco: ASP), ASP Conf. Ser., 411, 251
Mayor, M., & Queloz, D. 1995, Nature, 378, 355
Nikolov, N., Henning, T., Koppenhoefer, J., et al. 2012, A&A, 539, A159
Pollacco, D. L., Skillen, I., Collier Cameron, A., et al. 2006, PASP, 118, 1407
Pont, F., Zucker, S., & Queloz, D. 2006, MNRAS, 373, 231
Pont, F., Knutson, H., Gilliland, R. L., Moutou, C., & Charbonneau, D. 2008, MNRAS, 385, 109
Redfield, S., Endl, M., Cochran, W. D., & Koesterke, L. 2008, ApJ, 673, L87
Schneider, J., Dedieu, C., Le Sidaner, P., Savalle, R., & Zolotukhin, I. 2011, A&A, 532, A79
Seager, S. 2011, Exoplanets (Tucson, AZ: University of Arizona Press)
Seager, S., & Mallén-Ornelas, G. 2003, ApJ, 585, 1038
Seager, S., & Sasselov, D. D. 2000, ApJ, 537, 916
Sing, D. K., Pont, F., Aigrain, S., et al. 2011a, MNRAS, 416, 1443
Sing, D. K., Désert, J.-M., Fortney, J. J., et al. 2011b, A&A, 527, A73
Sing, D. K., Huitson, C. M., Lopez-Morales, M., et al. 2012, MNRAS, 426, 1663
Snellen, I. A. G., Albrecht, S., de Mooij, E. J. W., & Le Poole, R. S. 2008, A&A, 487, 357
Southworth, J., Mancini, L., Novati, S. C., et al. 2010, MNRAS, 408, 1680
Southworth, J., Bruni, I., Mancini, L., & Gregorio, J. 2012a, MNRAS, 420, 2580
Southworth, J., Mancini, L., Maxted, P. F. L., et al. 2012b, MNRAS, 422, 3099
Sozzetti, A., Torres, G., Charbonneau, D., et al. 2007, ApJ, 664, 1190
Swain, M. R., Vasisht, G., & Tinetti, G. 2008, Nature, 452, 329
Torres, G., Andersen, J., & Giménez, A. 2010, A&ARv, 18, 67
Tregloan-Reed, J., & Southworth, J. 2013, MNRAS, in press [arXiv:1212.0686]
Triaud, A. H. M. J., Queloz, D., Hellier, C., et al. 2011, A&A, 531, A24
Winn, J. N., Holman, M. J., Henry, G. W., et al. 2007, AJ, 133, 1828
Winn, J. N., Holman, M. J., Shporer, A., et al. 2008, AJ, 136, 267